

A combined X-ray, optical and radio view of the merging galaxy cluster MACS J0417.5-1154

M. B. Pandge,^{1*} R. Monteiro-Oliveira,^{2,3} J. Bagchi,⁴ A. Simionescu⁵,
M. Limousin^{6,7} and S. Raychaudhury^{4,8,9}

¹Dayanand Science College, Barshi Road, Latur, Maharashtra 413512, India

²Universidade Federal do Rio Grande do Sul, Instituto de Física, Departamento de Astronomia, 91501-970 Porto Alegre, Brazil

³Universidade de São Paulo, Inst. de Astronomia, Geofísica e Ciências Atmosféricas, Depto. de Astronomia, 05508-090 São Paulo, Brazil

⁴Inter-University Centre for Astronomy and Astrophysics, Post Bag 4, Ganeshkhind, Pune 411007, India.

⁵Institute of Space and Astronautical Science (ISAS), JAXA, 3-1-1 Yoshinodai, Chuo-ku, Sagami-hara, Kanagawa 252-5210, Japan

⁶Aix Marseille Univ, CNRS, LAM, Laboratoire d'Astrophysique de Marseille, Marseille, France

⁷Aix Marseille Univ, CNRS, CNES, LAM, Marseille, France

⁸Department of Physics, Presidency University, 86/1 College Street, Kolkata 700073, India

⁹School of Physics and Astronomy, University of Birmingham, Birmingham B15 2TT, UK

2 November 2018

ABSTRACT

We present a comprehensive multi-wavelength analysis of the merging galaxy cluster MACS J0417.5-1154 at a redshift of $z = 0.44$, using available images red obtained with *Chandra* in X-ray, *Subaru*, *Hubble Space Telescope* (HST) in optical, *Giant Metrewave Radio Telescope* (GMRT) in radio and *Bolocam* at 2.1 mm wavelength. This is an example of a complex merging galaxy cluster also hosting a steep-spectrum Mpc scale radio halo. The mass distribution obtained by weak lensing reconstruction shows that MACS J0417.5-1154 belongs to the dissociative class of mergers, where one of its substructures has had its gas content detached after the pericentric passage. We find the main cluster mass $M_{200} = 11.5^{+3.0}_{-3.5} \times 10^{14} M_{\odot}$ and the smaller second (sub)cluster mass to be $M_{200} = 1.96^{+1.60}_{-0.95} \times 10^{14} M_{\odot}$, leading to a large total mass of $M_{200} = 13.8^{+2.6}_{-2.8} \times 10^{14} M_{\odot}$. The overall structure, surface brightness profile, temperature and metal abundance of the intra-cluster medium (ICM) all point towards the presence of a cold front and merger induced gas-sloshing motion near the core. We detect a surface brightness edge to the south–east direction at a projected distance of ~ 45 arcsec (~ 255 kpc) from the centre of this cluster. The X-ray spectral analysis across the inner and outer edge allows us to confirm the detected edge as a cold front. The GMRT 235 MHz observation shows a comet–like extended synchrotron radio halo emission trailing behind the cold front. The peak of the Sunyaev-Zel'dovich decrement is found displaced from the centre of X-ray emission, which is interpreted as consequence of the merger dynamics. The optical HST imaging analysis of the cluster reveals the complex morphology of the BCG, with three surrounding ring-shaped structures with bright knots, which appear to be images of a multiply-imaged strongly lensed background galaxy. In addition two previously unknown giant arcs are found which are all indications of strong gravitational lensing in this massive system.

Key words: galaxies:active-galaxies:general-galaxies:clusters:individual:MACS J0417-1154-inter-cluster medium-X-rays:galaxies:clusters

1 INTRODUCTION

In the hierarchical scenario of structure formation in the Universe, galaxy clusters and their dark matter haloes grow by mergers of smaller subhaloes, representing galaxy groups

and subclusters, and by the accretion of dark matter and diffuse gas from the cosmic web (e.g. Eckert et al. 2015). A rare but important part of this process are the major mergers of galaxy clusters, which represent some of the most energetic events in the Universe, amounting to $E \geq 10^{64}$ ergs. The indicators of this process of growth and merging include features representing ram-pressure stripping and in-

* Email: mbpandge@gmail.com

stabilities (e.g., [Nulsen 1982](#)), shocks and cold fronts (e.g., [Markevitch & Vikhlinin 2007](#)), diffuse radio emission (e.g., [Feretti et al. 2012](#)), and significant offsets between the hot gas and dark matter substructures (e.g., [Clowe et al. 2004](#)). These merging galaxy clusters are thus excellent places to investigate some of the highest-energy phenomena known to us, including the physics of shock and cold fronts seen in diffuse intra-cluster medium (ICM), the cosmic ray acceleration in clusters, and the self-interaction properties of dark matter ([Bagchi et al. 2002](#); [Markevitch et al. 2004](#)).

Within this context we present the galaxy cluster MACS J0417.5-1154 (hereafter MACS0417). It is a hot ($T_{500} = 11$ keV)¹ galaxy cluster at $z = 0.443$ ([Caccianiga et al. 2000](#)). MACS0417 has a total (0.3–5 keV) X-ray luminosity and mass of $(29.1 \pm 0.5 \times 10^{44})$ ergs⁻¹ and $(22.1 \pm 3.9 \times 10^{14})$ M_⊙ respectively, within R_{500} ([Piffaretti et al. 2011](#)) and it is one of the clusters included in the Reionization Lensing Cluster Survey (RELICS; [Coe & RELICS Team 2017](#)).

MACS0417 hosts a ~ 1 Mpc scale radio halo that was first reported by [Dwarakanath et al. \(2011\)](#), and more recently explored in detail by [Parekh et al. \(2017\)](#) using observations with the *Giant Metrewave Radio Telescope* (GMRT) at 235 MHz, 610 MHz, and the Jansky Very Large Array (JVLA) at 1575 MHz and with *Chandra* in X-rays. The extended radio halo of the cluster is coincident with the hot X-ray gas.

The X-ray analysis of this cluster, based on *Chandra* observations, has revealed a distinct comet like morphology of the diffuse emission, with a compact core that is extremely X-ray bright ([Mann & Ebeling 2012](#)). A combined X-ray and optical study of [Mann & Ebeling \(2012\)](#) reported the possibility of a shock front in this system.

A close look at the spatial distribution of the various components of a galaxy cluster can help to characterise its dynamical status. Whereas the distribution of the hot gas is traced by its X-ray emission, the dark matter component (which corresponds to upto 80% of the total cluster mass) can be mapped from its gravitational influence, imprinted in the distortion in the shapes of background galaxies seen beyond the cluster, mapped in the form of weak lensing. In the case of MACS0417, the cluster was included in the *Weighing the Giants* sample ([von der Linden et al. 2014](#); [Applegate et al. 2014](#)), but in spite of the clear signs of a disturbance, MACS0417 was treated as a single structure in this study, which yielded $M(< 1.5 \text{ Mpc}) = 18.9_{-2.5}^{+2.6} \times 10^{14}$ M_⊙, indicating that MACS0417 is a very massive system.

In this paper, we present a detailed multi-wavelength analysis of MACS0417 by combining the existing *Chandra* X-ray observations with *Subaru* and Hubble Space Telescope (HST) optical archival observations. Our weak lensing modelling, the first in the literature accounting for multiple components in this target, has provided a detailed anatomy of the merging system. This significantly enhances the opportunity to perform a comparison between the spatial distribution of the cluster components: member galaxies, intra-cluster medium and dark matter. We also detect several

strong lensing features, that have not been pointed out before, in the HST archival images.

In section § 2, we outline the observations and data reduction strategy, which includes X-ray, radio and optical imaging. The weak lensing analysis and its results are fully described in section § 3, while in § 4, we describe merging signature at other wavelengths. In section § 5 and section § 6 we discuss these results in their broader context, and outline our main conclusions.

Throughout the paper, we adopt a Λ CDM cosmology with $H_0 = 70$ km s⁻¹ Mpc⁻¹, $\Omega_m = 0.3$, and $\Omega_\Lambda = 0.7$, in which, 1' at the redshift of MACS0417 corresponds to ≈ 340 kpc. Unless specifically mentioned otherwise, errors are quoted at the 90% confidence level.

2 OBSERVATIONS AND DATA REDUCTION

2.1 Subaru observations

For the weak lensing analysis, one requires deep images, with a large field of view, in order to map the lensed background galaxies. Multi-band observations with SuprimeCam centred on MACS0417 were obtained from the Subaru telescope archives² (see Table 1). The image reduction process used the usual semi-automated pipeline SDFRED ([Ouchi et al. 2004](#); [Yagi et al. 2002](#)), involving bias and overscan subtraction, flat-fielding, atmospheric and dispersion correction, sky subtraction, auto-guide masking and alignment (simultaneously for all three filters). The images were then combined and mosaicked into a final image for each filter by registering the sub-images with IRAF. Photometric calibrations in the AB system ([Oke 1974](#)) were performed by comparing the images with the relevant standard star catalogue ([Zacharias et al. 2004](#)). Our final image of 37.6×36.4 arcmin is sufficiently large for our purposes, enabling us to access regions at large projected distances from the centre of the cluster.

Object catalogues were constructed using SExtractor ([Bertin & Arnouts 1996](#)) in “double image mode”, having as reference the image in the R_c filter. Galaxies were identified according to two complementary criteria: for magnitudes $R_C \geq 18.0$, galaxies were defined as the objects with FWHM > 1.15 arcsec, and for the brighter objects ($R_C < 18$), galaxies were identified as having SExtractor’s CLASS_STAR < 0.8 . Stars were likewise selected by their stellarity index or their FWHM.

2.2 Chandra X-ray observations

MACS0417 was observed with *Chandra* twice, in VFaint mode, between 28 to 29 October 2009, for a total of 80 ks. The observations were analyzed using CIAO v4.8, with CALDB V4.6.5. The data reduction steps are the same as those employed in the analysis of the *Chandra* data of MACS0553.4-3342 ([Pandge et al. 2017](#)). Soft proton flares were removed from the data, point sources were subtracted, and the rescaled instrumental backgrounds (to ensure that their count rates in 10 – 12 keV are the same as the count rates of the observations in the same energy band) were

¹ T_{500} refers to the temperature measured in a circle of radius R_{500} , within which the mean mass density is 500 times the critical density of the Universe at the cluster redshift.

² <http://smoka.nao.ac.jp/>

Table 1. Subaru SuprimeCam imaging characteristics.

Date	Band	Images	Total exposure (min)	Seeing (arcsec)
12-12-2001	<i>V</i>	6	24	1.6
12-12-2001	<i>I</i>	1	4	1.6
02-23-2004	<i>R_C</i>	6	24	1.1
02-24-2004	<i>I</i>	6	18	1.0

subtracted from the images and spectra. The X-ray point sources were detected using the CIAO task WAVDETECT with scales of 1, 2, 4, 8 pixels, detected at 3σ above the background, with an absolute detection threshold of 10^{-6} . The missing patches left after point source removal were replaced with the mean surface brightness level of their surroundings to image the diffuse X-ray emission around the cluster. The regions covered by the compact point sources were simply excluded from the spectral extraction regions. A summary of the two ObsIDs used in this paper is presented in Table 2.

2.3 Radio data

MACS0417 was also observed with the *Giant Metrewave Radio Telescope* (GMRT) at 235 and 610 MHz in the dual-frequency mode during 2010 October by Dwarakanath et al. (2011). These observations had led to the discovery of a steep spectrum radio halo, but no signatures of merger shock driven radio relics are seen in the outskirts of this cluster, unlike other extreme merging systems (Bagchi et al. 2011; Kale & Dwarakanath 2012; van Weeren et al. 2016). More information related to the radio data and reduction can be found in (Parekh et al. 2017). For the present study we use the GMRT 235 MHz radio data.

2.4 Hubble Space Telescope observations

MACS0417 has been imaged with the Hubble Space Telescope (HST) with various broadband filters. In this paper we have used archival data in the F606W (closest to the *V* band; PI: van der Linden) and the F160W (closest to the *H* band; PI: Dan Coe) filter images, for an effective exposure time of 1910 and 1005 sec, respectively. These images have been used to determine the morphology of the brightest cluster galaxy (BCG) and to look for strong gravitational lensing features.

2.5 Bolocam observations

MACS0417 has been also imaged with the Bolocam 2.1 mm wavelength (140 GHz) Galaxy Cluster survey (<http://irsa.ipac.caltech.edu>) (Sayers et al. 2013), which reveals a strong Sunyaev-Zel'dovich effect (SZE) decrement signal. Bolocam comprises of a 144-element bolometer array at the Caltech 10.4m Submillimeter Observatory, at Mauna Kea, Hawaii, with a beam of $58''$ (FWHM) at 140 GHz and a circular field-of-view of diameter 8 arcmin. In the present analysis we used publicly-available, filtered SZE images from this survey, of which more can be found in section § 4.3 below.

3 WEAK GRAVITATIONAL LENSING ANALYSIS

3.1 Basic concepts

In the reconstruction of the distribution of matter using gravitational lensing, the weak regime corresponds to the linear manifestation of the lensing, which cannot be measured using the effect on a single galaxy. Thus, this phenomena must be quantified in a statistical manner. Formally, the gravitational lensing field is described by a scalar quantity, the convergence (κ), plus a spin-2 tensor, the shear ($\gamma = \gamma_1 + i\gamma_2$), where $\gamma_1 = |\gamma| \cos(2\theta)$ and $\gamma_2 = |\gamma| \sin(2\theta)$ (θ is the shear direction), both being related to the second derivatives of the projected gravitational potential (e.g. Mellier 1999; Schneider 2005; Kneib & Natarajan 2011). For circularly symmetric systems, the shear components are described in terms of a tangential component (in relation to the lens centre), frequently called γ_+ , and another at 45 deg with respect to it, known as γ_\times .

Physically, the convergence κ is directly related to the projected surface mass density of the lens, in units of the lensing critical density

$$\Sigma_{cr} = \frac{c^2}{4\pi G} \frac{D_s}{D_{ds}D_d}, \quad (1)$$

with D_s , D_{ds} and D_d being the angular diameter distances to the source (i.e. background objects with respect to the lens), between the lens and the source, and to the lens, respectively. The domain of the weak lensing regime can now be defined as the projected regions in the image where we find $\kappa \equiv \Sigma/\Sigma_{cr} \ll 1$. Geometrically, the convergence is responsible for an isotropic magnification of the sources.

In an unlensed sample, the value of average source ellipticity is expected to be zero. The lensing effect, however, results in coherent distortions in these images in a way that the average ellipticity will tend to the effective shear or distortion g ,

$$\langle e \rangle \simeq g \equiv \frac{\gamma}{1 - \kappa}, \quad (2)$$

where the ellipticity modulus, in terms of the semi-major axis a and semi-minor axis b , is defined as

$$e = \frac{a - b}{a + b}. \quad (3)$$

The so-called full ellipticity (as well as the shear and the effective shear) cannot be defined by its modulus only, because it also has an orientation (θ , i.e., the direction of the semi-major axis). It is commonly described as a spin-2 tensor (a ‘‘headless’’ vector), whose two components can be defined as

$$e_1 = e \times \cos(2\theta) \quad \text{and} \quad e_2 = e \times \sin(2\theta). \quad (4)$$

Table 2. *Chandra* Observation log

ObsID	Observing Mode	CCDs on	Starting Date	Total Time (ks)
11753	VFAINT	0,1,2,3,6	2009-10-28	54
12010	VFAINT	0,1,2,3,6	2009-10-29	26

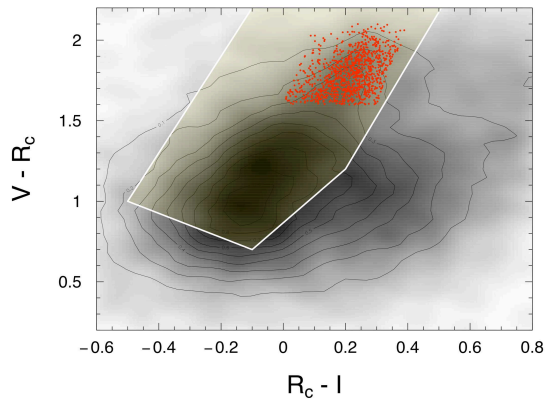


Figure 1. Colour-colour diagram of the selected galaxies in the Subaru optical images. Black thin lines represent the density of galaxies, while red cluster member galaxies (red points) were found through a statistical subtraction process (e.g. Monteiro-Oliveira et al. 2017b). Departing from Medezinski et al. (2010) criteria, we have identified the locus preferentially occupied by the foreground population (yellow central region) in the sense that all galaxies outside this region were considered as part of the background sample if $R_C > 23$.

3.2 Identifying the galaxy populations

The *locus* occupied by the red cluster members in the colour-colour (CC) diagram (e.g. Medezinski et al. 2010) was delineated using a statistical subtraction process, outlined in detail in Monteiro-Oliveira et al. (2017b). We have compared an inner region at the core of the cluster MACS0417 ($\sim 6 \times 6$ arcmin), with two outer regions (25×8 arcmin each) near the image border. We found that the galaxy counts identified by the above process in the core of the cluster were higher than the counts in the peripheral regions of the Subaru image up to $R_C = 23$, which was considered to be the brightest limit for the detected background (source) galaxies. These source galaxies are expected to occupy a region, in the CC diagram, that is complementary to the cluster members and the foreground sample (see Fig. 1).

While the weak lensing technique relies only on the background galaxy sample, we can compare further the mass distribution (dominated by the dark matter component), with the spatial distribution of cluster member galaxies. The resulting numerical density distribution, and the same quantity weighted by the R_C luminosity for 1014 identified red sequence galaxies, are shown in Fig. 2 (“B” and “C” respectively). In both cases, we see a bimodal distribution, closely following the ICM distribution sampled by their X-ray emission (“A”). Moreover, each BCG is located near to the closest region of higher density. Hereafter, we will refer to the clump related to the 1st BCG (on the southeastern side) as

the “main cluster” and to the 2nd BCG as “subcluster” (on the northwestern side).

3.3 Shape measurements

Atmospheric blurring, combined with the angular response of telescope optics and instrumentation, transforms the images of point-like stars into extended images. This is quantified by the point spread function (PSF), which is characterised with the help of the images of bright and unsaturated stars.

The weak lensing exercise is based on shape measurements of the background galaxies, for which the PSF deconvolution were performed with the Bayesian code IM2SHAPE (Bridle et al. 1998)³, which models an image as a sum of Gaussians, with elliptical kernels.

To find the PSF parameters (ellipticity components e_1 , e_2 and the FWHM), unsaturated stars are modelled as single Gaussian profiles: for these, no deconvolution is performed. Then the discrete values are turned continuous over the image using the thin plate spline regression (TPS, Nychka et al. 2014). Smooth PSF parameter surfaces were reached here by setting $df = 20$ parameters in the TPS configuration. Aiming to remove the objects with large residuals, this process is iterated three times, removing in each interaction 10% of the objects with the largest discrepancy. The final measured ellipticities, as well the corresponding residuals, are shown in Fig. 3. This PSF is then used to model the shapes of the source (background) galaxies.

We have deconvolved the local PSF to recover the distortion induced by the gravitational lens (there is also the effect of the unknown original shape, but it can be overcome later). As an additional precaution, we have excluded from the final sample the galaxies with large ellipticity errors ($\sigma_e > 2$) and with evidence of contamination from nearby objects. Our final background lensed galaxies consisted of 8950 objects giving a projected density of ~ 6 gals. arcmin⁻².

The average lensing critical surface density Σ_{cr} (Eq. 1) was estimated by comparing our previous applied magnitude and colour cuts (Fig. 1) in the COSMOS photometric redshift catalogue (Scoville 2007). Due to the absence of R_C and I bands in the survey, we have considered as proxy the filters r' and i' respectively. After this procedure we found $\Sigma_{cr} = 2.00(5) \times 10^9 M_\odot \text{ kpc}^{-2}$.

3.4 Mass reconstruction and modelling

We have used the code LENSENT2 (Marshall et al. 2002) designed to minimise a χ^2 -like statistical quantity, based on the comparison between the measured ellipticities with those predicted by the model (see also Seitz et al. 1998). As an

³ <http://www.sarahbridle.net/im2shape/>

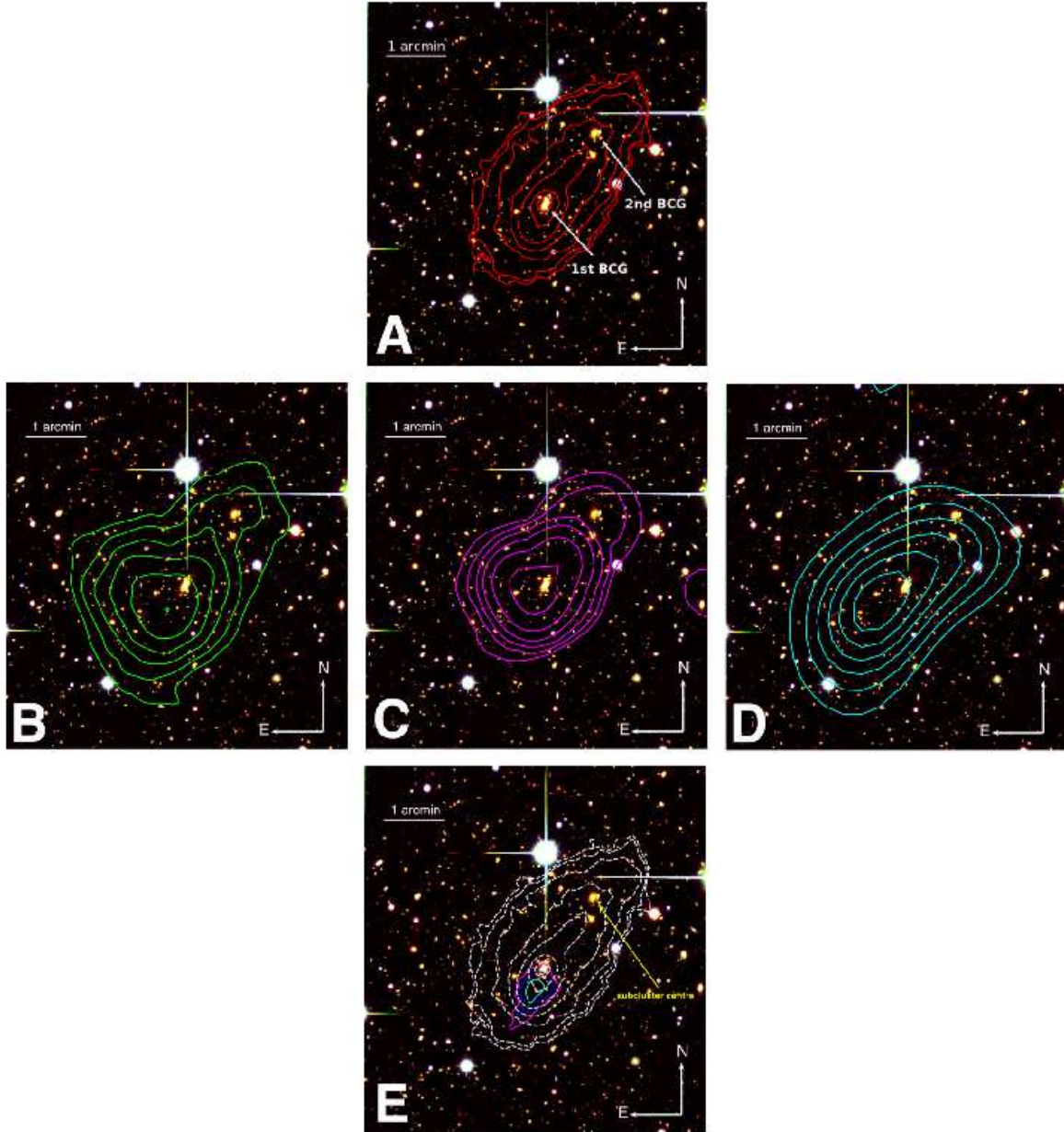


Figure 2. The combined V , R_C and I images of the merging galaxy cluster MACS0417 observed with SuprimeCam mounted on the Subaru telescope. The optical image is overlaid with (A) *Chandra* X-ray contours, (B) the logarithm of the numerical density distribution of the cluster red member galaxies, (C) the logarithm of the numerical density distribution weighted by the R_C luminosity, (D) total mass distribution obtained by LENSENT2, where the contours are linearly spaced by 0.04 within the interval $\kappa \in [0.14 : 0.38]$ and (E) 1σ (cyan), 2σ (blue) and 3σ (magenta) confidence contours of the position of mass centre, and the ICM distribution traced by its X-ray emission (dotted white lines). The unimodal logarithmically spaced X-ray contours are nearly aligned with the axis connecting the two BGCs, which indicated that this might be the direction of the projected merger axis. The numerical density distributions are very similar, and show a bimodal structure roughly centred on the respective BGCs. The recovered total mass closely follows the ICM distribution, also showing a unimodal peak. Finally, the modelled cluster mass centre (keeping the subcluster centre fixed at the 2nd BCG) shows a spatial agreement within 99% confidence limit, between the 1st BCG and the X-ray peak, showing that this structure has not suffered a displacement of the bulk of the ICM.

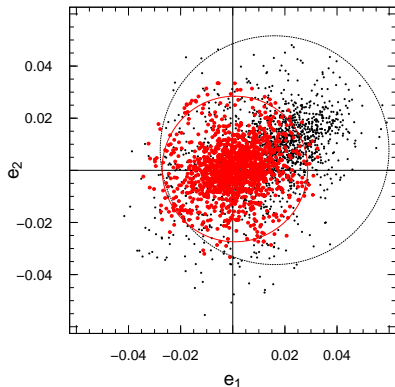


Figure 3. Modelling of the PSF based on bright and unsaturated stars. *Black* points: the initial e_1 , e_2 distribution with $\langle e_1 \rangle = 0.014$, $\sigma_{e_1} = 0.017$ and $\langle e_2 \rangle = 0.006$, $\sigma_{e_2} = 0.015$. If the stars were observed as real point sources we would expect $\langle e_1^* \rangle = \langle e_2^* \rangle = 0$ so that the deviation is directly related to the PSF effect. *Red* points: the residual distribution after the iterative process to quantify the PSF along the field with $\langle \text{res} \rangle_{e_1} = 0$, $\sigma_{\text{res}_{e_1}} = 0.013$ and $\langle \text{res} \rangle_{e_2} = 0$, $\sigma_{\text{res}_{e_2}} = 0.012$. The *circles* enclose 95% of the points.

additional input, the code requires a smoothing scale to account for the fact that each galaxy is not isolated, i.e., they are correlated with those in their vicinity. We have adopted $\sigma = 80$ arcsec as used for the numerical density maps (Fig. 2 “B” and “C”).

The resulting mass distribution, presented in Fig. 2 “D”, shows a strong similarity with the maps of X-ray and galaxy number density. Although it does not appear clearly bimodal, the mass distribution is elongated along the line joining the two BCGs. This could be a hint that MACS0417 represents two subclusters with widely different masses, and that the lensing signal of the (much) lighter subcluster cannot be detected with the same contrast as that of the more massive partner.

The mass distribution in the cluster field was modelled as two lenses, each one following a NFW (Navarro et al. 1996, 1997) profile (Wright & Brainerd 2000), which essentially requires four parameters: the mass scales (M_{200}^c , M_{200}^s) and the respective halo concentrations (c^c , c^s). In addition, the parametrization of each halo depends on the position of their centre (x, y) , which can be also included as a free parameter (e.g. Monteiro-Oliveira et al. 2017a). However, increasing the number of parameters yields output quantities which are less constrained. In the following, we will implement strategies to diminish the number of final parameters.

The halo concentration was fixed based on the mass-concentration relationship presented by Duffy et al. (2008),

$$c = 5.71 \left(\frac{M_{200}}{2 \times 10^{12} h^{-1} M_{\odot}} \right)^{-0.084} (1+z)^{-0.47}, \quad (5)$$

where z is the redshift of MACS0417. As suggested by Fig. 2 (“D”), the subcluster appears to be overwhelmed by the main cluster, which indicates that we might not be able to fit simultaneously both the mass and the position of the centroid of the subcluster. In fact, initial tests have shown that keeping the subcluster centre as a free parameter dramatically increases the error bar in the other parameters and

returned non-convergent results. We decided then to adopt the reasonable assumption that the centroid of mass of the subcluster is coincident with the 2nd BCG, as suggested by the numerical density map of the red members (Fig. 2 “B” and “C”). After these considerations, our fiducial model was reduced to 4 unknown parameters: M_{200}^c , M_{200}^s , x^c , y^c , where the index “c” refers to the main cluster and “s” to the subcluster.

Due to the absence of circular symmetry (since we are simultaneously modelling two halo profiles), we worked with Cartesian components of the effective shear rather than the usual tangential components. The transformation is done just by multiplying g_+ by the lensing convolution kernel,

$$D_1 = \frac{y^2 - x^2}{x^2 + y^2} \quad \text{and} \quad D_2 = \frac{2xy}{x^2 + y^2}, \quad (6)$$

where x and y are the Cartesian coordinates relative to the respective lens centre.

The total effective shear calculated at each lensed galaxy position can be written as a sum of the contribution of each halo,

$$g_i = g_i^c + g_i^s, \quad i \in \{1, 2\}. \quad (7)$$

The model prediction is then compared to the measured ellipticities e_1 and e_2 for the N background sources through the χ^2 ,

$$\chi^2 = \sum_{j=1}^N \sum_{i=1}^2 \frac{(g_i - e_{i,j})^2}{\sigma_{int}^2 + \sigma_{obs,i,j}^2}, \quad (8)$$

with $\sigma_{obs,i,j}$ being the errors reported by IM2SHAPE, and σ_{int} the uncertainty associated with the intrinsic ellipticity distribution of the source galaxies, estimated as 0.35 for our dataset.

Finally, the posterior can be written as

$$\Pr(M|\text{data}) \propto \mathcal{L}(\text{data}|M) \times \mathcal{P}(M). \quad (9)$$

A uniform prior $\mathcal{P}(M) : 0 < M_{200} \leq 9 \times 10^{15} M_{\odot}$ was adopted to allow the chains to quickly reach the stationary state. For data normally distributed around the model, the likelihood is related to the previous χ^2 statistics as

$$\ln \mathcal{L} \propto -\frac{\chi^2}{2}. \quad (10)$$

3.5 Results

The posterior of the problem (Eq. 9) was evaluated by an MCMC (Markov chain Monte Carlo) algorithm with a simple Metropolis sampler implemented in the R function MCMCMETROP1R (Martin et al. 2011). We generated four chains of 1×10^5 points, added with the first 1×10^4 points as “burn-in” iterations, to ensure that the chains fully represent the stationary state. To check the final combined chain convergence, we also measured the potential scale factor R , as implemented in the CODA package which has shown that the convergence cannot be discarded within 68% confidence limit ($R \leq 1.0$).

The final posterior of the mass measurements is shown in Fig. 4. The main cluster and subcluster masses, marginalized over the other parameters, are presented in Tab. 3. Concerning these values, the previous speculation about the high mass ratio of MACS0417 is plausible according

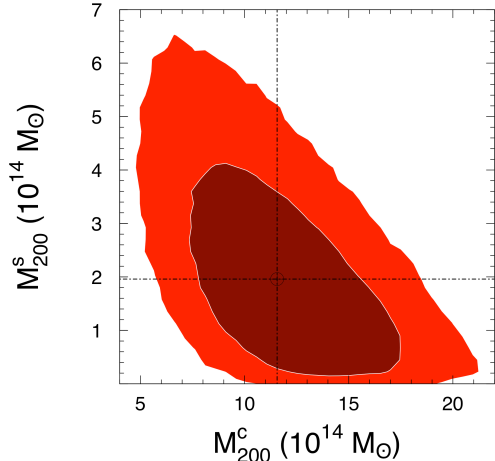


Figure 4. Marginalized posterior of the main cluster (c) and subcluster (s) masses. The crimson area corresponds to a confidence level of 68% whereas the lighter red area covers up to the level of 95%. The individual values (dashed-dotted lines), corresponding to the median of each distribution, are listed in Tab. 3. We found the Spearman correlation coefficient between the two parameters to be $\rho = -0.5484 \pm 0.0011$.

Table 3. Mass modelling results. The representative values correspond to the median of each marginalized PDF. The error bars refer to 68% c.l.

	M_{200} ($10^{14} M_{\odot}$)
Main cluster (c)	$11.5^{+3.0}_{-3.5}$
Subcluster (s)	$1.96^{+1.60}_{-0.95}$
Total (c+s)	$13.8^{+2.6}_{-2.8}$

to our model which indicates a ratio $\sim 6:1$, considering the representative median values, pointing that the system has been experiencing a minor merger (Martel et al. 2014). Actually, this classification is consistent with 67% of the realizations, whereas in $\sim 9\%$ the scenario is better described as a major merger (i.e. the mass ratio is less than 2:1). The corresponding total mass⁴ is $M_{200} = 13.8^{+2.6}_{-2.8} \times 10^{14} M_{\odot}$ inside $R_{200} = 1.96 \pm 0.14$ Mpc. These values are found to be practically unchanged, when we used a conservative model, keeping both the main cluster and subcluster mass centres fixed at their corresponding BCGs. Besides, our total mass estimation agrees within the error bars with those obtained by Applegate et al. (2014), $M(< 1.5 \text{ Mpc}) = 18.9^{+2.6}_{-2.5} \times 10^{14} M_{\odot}$, in spite of the fact that their model considers MACS0417 to be a single cluster.

The confidence contours of the modelled main cluster mass centre are presented in Fig. 2 “E”. This figure also enables us to make a comparison between the 1st BCG and the X-ray peak positions. As seen, for example, in the merging galaxy clusters A1758 (Monteiro-Oliveira et al. 2017a) and A3376 (Monteiro-Oliveira et al. 2017b), we notice no signif-

icant offset among the main cluster components, meaning that the structure has retained its gas content after the collision with the subcluster. In fact, both locations of the X-ray peak and the 1st BCG are consistent with the position of the mass centre within 99 % c.l. As far as the subcluster is concerned, the X-ray map (Fig. 2 “A”) shows no evidence of a related emission peak, suggesting that it was previously disrupted due to the large-scale collision (as seen for example in the merging cluster A3376; Monteiro-Oliveira et al. 2017b).

4 MERGING SIGNATURES AT OTHER WAVELENGTHS

4.1 X-ray

4.1.1 Imaging analysis

In Fig. 5, we show the X-ray surface brightness map of the diffuse emission of the ICM of the cluster, in the energy band 0.5–3 keV for the *Chandra* observation. The image has been corrected for exposure and vignetting, with the instrumental background subtracted, and it has been smoothed with a Gaussian kernel of width 1 arcsec. From visual inspection of this image, it is evident that the appearance of MACS0417 cluster has a comet-like morphology, with a bright core in the X-rays. This morphology clearly indicates that a high velocity encounter occurred in this system, similar to that in the Ophiuchus Cluster (Million et al. 2010) and Abell 2146 complex (Rossetti et al. 2013). Apart from the bright X-ray core, the image reveals a tail-like feature directed towards the north-east (hereafter NE) and another interesting sharp edge-like feature evident to the south-east (hereafter SE) from the centre of the cluster. There is a clear indication of a surface brightness discontinuity/edge along the SE direction. To detect and confirm the surface brightness edge, we have used various image analysis techniques, which we discuss in detail below.

4.1.2 Surface Brightness Profiles

X-ray surface brightness profiles can reveal features like surface brightness edges, pre- and post-shock signatures, cold fronts and other attributes of merging events seen in galaxy clusters. We derived surface brightness profiles from the *Chandra* observation, by extracting X-ray counts from four sectors, from the centre of MACS0417 as shown in Fig. 6. The sectors and angles (measured counter-clockwise from the Right Ascension axis) used to extract the surface brightness profiles are given in the inset of Fig. 6.

This figure clearly shows an excess X-ray emission across the position angle (0° – 90°) (colour: black) within the range of 20 arcsec to 2 arcmin in radius. In the same figure, the profile extracted from the SE direction, covering the position angle (180° – 270°) (colour: green) also shows excessive X-ray emission in the range of radial distance between 0.1–0.5’ in this sector, compared with the similar range in other profiles. Further, the surface brightness drops abruptly at 0.5’, beyond which its behaviour is similar to the surface brightness profiles at other ranges in azimuth. This indicates the possible presence of a density discontinuity in this direction.

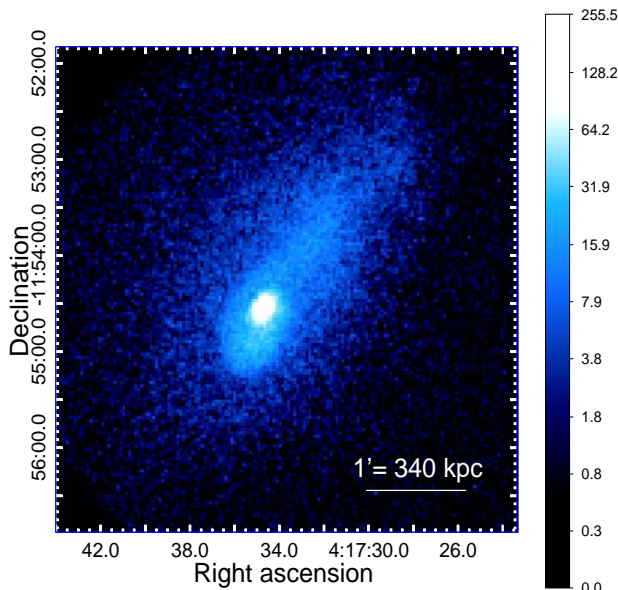
⁴ Taken as the median of the sum of both main and subcluster individual posteriors.

Table 4. Best-fit values of the broken power-law density model

Angle	α_1	α_2	r_{sh} (arcmin)	n_0 (10^{-4}cm^{-3})	C	χ^2/dof
($180^\circ-270^\circ$)	0.46 ± 0.04	1.19 ± 0.11	0.72 ± 0.03	9.1 ± 0.59	2.21 ± 0.12	78.81/33

Table 5. Best fit spectral properties of the T2 and T1 regions shown in Fig. 7.

Reg.	Net Counts	N_H 10^{20}cm^{-2}	kT (keV)	Z Z_\odot	Norm (10^{-4}) (cm^{-3})	P (10^{-2}KeVcm^{-3})	χ^2 (d.o.f.)
T2	3160	7.12 ± 0.13	$7.20^{+1.38}_{-0.99}$	0.54 ± 0.14	4.10 ± 0.16	4.96 ± 0.92	62.98 (65)
T1	1350	8.71 ± 0.06	$16.37^{+6.89}_{-4.35}$	0.97 ± 0.79	1.56 ± 0.20	4.86 ± 1.20	34.23 (39)

**Figure 5.** X-ray (*Chandra*) log scaled surface brightness map of MACS0417 in the energy band 0.5 – 3.0 keV. The image was corrected for exposure, vignetting, and after subtracting point sources and the instrumental background, was smoothed with a Gaussian kernel of width 1 arcsec (2 pixels).

4.1.3 A SE Surface brightness edge

We further investigated the possible density discontinuity by extracting a surface brightness profile using an elliptical sector with covering the position angle ($180-270^\circ$), fixing ratio between major and minor axis ~ 1.13 and shown by dashed lines in Fig. 7 (*left panel*). The surface brightness profile across the edge, shown in the right panel, was fitted with a broken power-law density model. The broken power-law density model was parametrized as:

$$n(r) = \begin{cases} C n_0 \left(\frac{r}{r_{sh}}\right)^{-\alpha_1}, & \text{if } r < r_{sh} \\ n_0 \left(\frac{r}{r_{sh}}\right)^{-\alpha_2}, & \text{if } r > r_{sh} \end{cases} \quad (11)$$

where n is the electron number density, n_0 is the electron density normalization, C is the density compression, α_1 and

α_2 are the power-law indices, and r_{sh} is the radius of the density jump. We binned the profile to have approximately 28 counts/bin and fitted it with the `PROFFIT` package V1.4 (Eckert et al. 2011). The best-fitting parameters are summarized in Table 4.

This modelled density was squared and integrated along the line of sight, assuming an isothermal plasma and a ellipsoidal geometry.

4.1.4 Nature of the SE edge revealed by spectral analysis

To better understand the nature of the SE density discontinuity, we extract the spectra from two “PandA”s (inner T2 and outward T1), shown in blue in Fig. 7 (*left panel*). The background spectra were also extracted from similar regions from the blank sky background file (see Pandge et al. 2017). The extracted spectra were binned (28 counts/bin), then exported to `XSPEC`, and fitted with a simple single temperature model `wabs*apec`, keeping the redshift values fixed at $z = 0.44$. The Galactic N_H value was kept free during the fit. The best fit parameters were derived using χ^2 minimisation and the errors were derived for the 90% confidence level. The obtained best fit Galactic N_H values are factor of 2.26 higher than that of reported by (Dickey & Lockman 1990). The best fit parameters are tabulated in Table 5. Considering the values of the quantities n_2/n_1 and $T1/T2$ across the surface brightness edge, we find that the gas pressures across both sides of the SE edge are consistent within the errors. Therefore, we classify this edge as a cold front. It turns out to be similar to typical sloshing cold fronts seen in many other systems (see Markevitch & Vikhlinin 2007, for review). At the time of revising this paper, another paper on MACS0417 appeared on arXiv, containing analysis of the *Chandra* observations (Botteon et al. 2018). This paper has also reported this jump with $C = 2.44 \pm 0.31$, which is consistent with our detection.

4.2 Radio

In order to further investigate the connection between the radio and the X-ray emitting gas distributions, we overlay the GMRT 235 MHz radio contours on the exposure-corrected and background-subtracted *Chandra* X-ray surface bright-

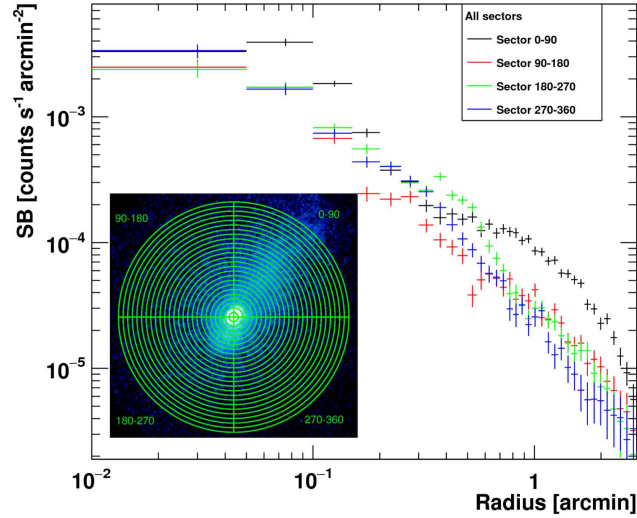


Figure 6. The extracted X-ray surface brightness profiles across four sectors from the centre of MACS0417. The sectors and the angles (measured counter-clockwise from the Right ascension axis) used to extract the surface brightness profiles are shown in the inset.

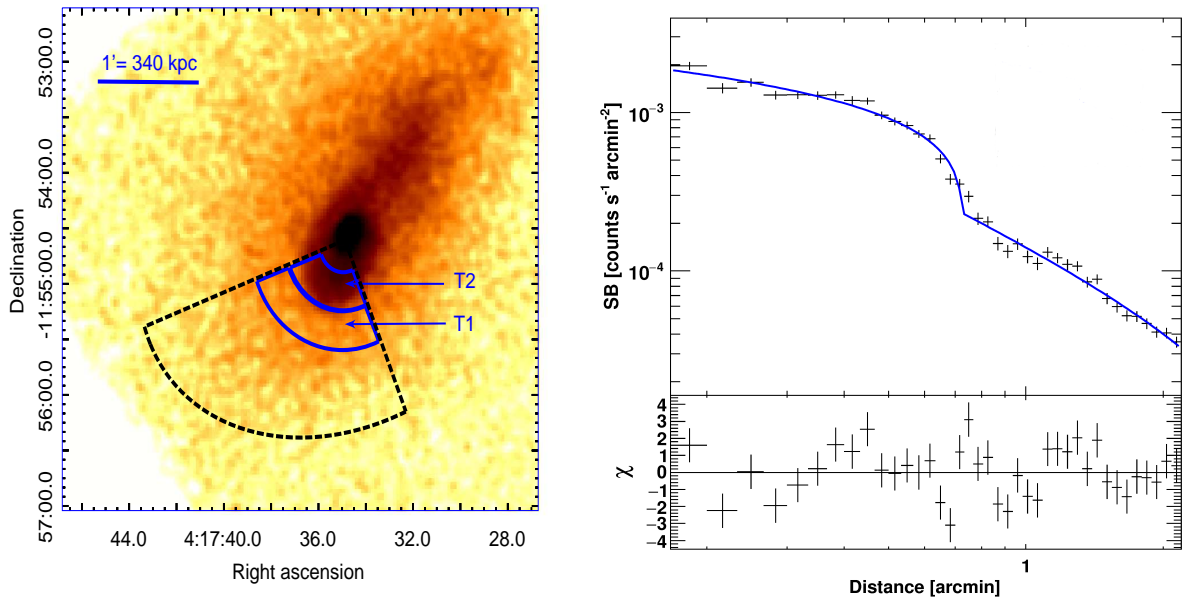


Figure 7. *left panel:* The *Chandra* X-ray (0.5–3.0 keV energy band) image on which the sector, used to extract the surface brightness profile across the SE edge, has been overlaid. The far inner regions, T2 and T1, were used to extract the spectrum across the detected surface brightness edge. *Right panel:* Best-fit broken power-law density model (solid blue line) for the surface brightness edge extracted from 180°–270° from the centre of the cluster. The surface brightness profile is instrumental background subtracted.

ness image, shown in Fig. 8. This figure shows that the radio contours of MACS0417 are elongated in the SE-NW direction, closely following the X-ray emission. The 235 MHz GMRT observation shows extended radio emission within

the SE cold front (magenta arc), as seen in some clusters hosting a diffuse radio mini-halo.

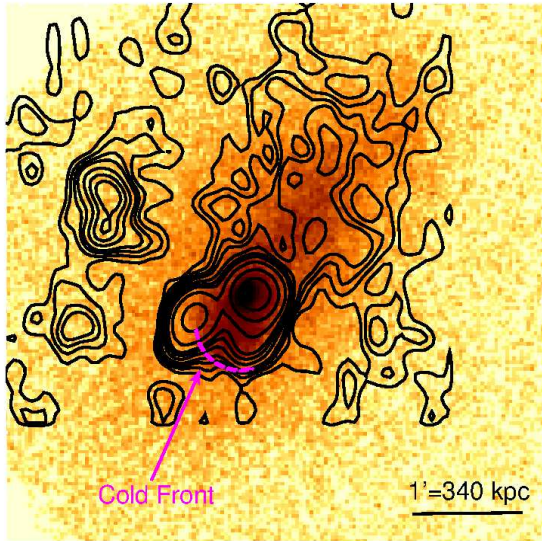


Figure 8. *Chandra* X-ray (0.5–3.0 keV energy band) surface brightness image on which the GMRT 235 MHz radio contours are overlaid. The position of detected cold front (dashed magenta coloured arc) is shown by an arrow.

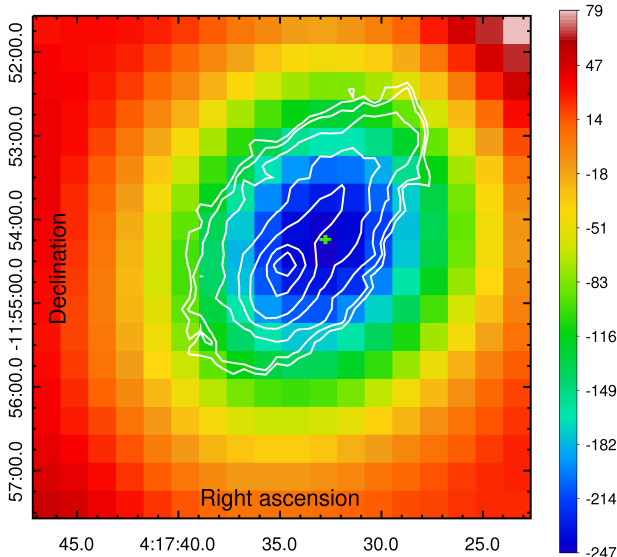


Figure 9. The Sunyaev-Zel'dovich Effect (SZE) decrement, filtered map, at 2.1 mm wavelength (6 arcmin \times 6 arcmin field) of the MACS0417 cluster obtained from the Bolocam archives. The *Chandra* X-ray surface brightness (white) contours have been overplotted on it for comparison. The green cross indicates the peak decrement position of the 2.1 mm SZE map.

4.3 Sunyaev Zel'dovich Decrement

Here we examine the available Sunyaev-Zel'dovich Effect (SZE) decrement images for MACS0417, as the total cluster SZE signal is a good proxy for the total mass (e.g., Nagai 2006), and is known to trace extremely well the thermal pressure of the ICM. We use a publicly-available filtered SZE image from the Bolocam survey (Sayers et al. 2013). The final 6 arcmin \times 6 arcmin, filtered Sunyaev-Zel'dovich map, at a

wavelength of 2.1 mm, is shown in Fig.9. The *Chandra* X-ray surface brightness (white contours) have been overplotted on this image for comparison. The green cross indicates the peak SZE decrement position at RA $04^h 17^m 32.14^s$, Dec. $-11^\circ 54' 7.70''$. The *Chandra* X-ray emission peak is located at RA $04^h 17^m 34.86^s$, Dec. $-11^\circ 54' 34.04''$. From this comparison, it is revealed that the strong Sunyaev-Zel'dovich decrement peak ($\Delta T \approx 500$ mK) is offset by $\sim 50''$ (~ 275 kpc) to the north-west of cluster X-ray centre in the direction of the radio halo extension. We note that the pointing accuracy of Bolocam instrument is 3 rms while for *Chandra* X-ray telescope absolute position has a error radius of 0.8 arcsec (90% uncertainty circle), and both are much smaller than the significant SZ - X-ray positional offset detectable. However, a caveat is that some centroid shift can also be introduced by the broad $\sim 60''$ (FWHM) beam of the Bolocam observation. Thus, a much finer resolution SZE observation is required to measure the SZ - X-ray offset with higher accuracy. The origin of this offset can possibly be traced to the strong merging dynamical state of MACS0417, where the X-ray surface brightness maxima ($I_x \propto \rho_g^2 T_g^{1/2}$) shifts to a region of the highest gas density (ρ_g) near the cold-front, while the SZE peak ($I_{SZ} \propto \rho_g T_g$) traces the region of highest thermal pressure of a subcluster, offset from the former due to merger dynamics.

4.4 Strong Lensing

We now investigate in more detail the $\sim 30 \times 30$ arcsec² ($\sim 170 \times 170$ kpc²) central region of MACS0417, using the *Chandra* X-ray and the high-resolution (0.05 arcsec/pix) optical images from the HST. The resultant images are shown in Fig. 10 (panels A and C). The *Chandra* image (panel A) shows that the X-ray isophotes are elliptical in shape (the peak X-ray position is highlighted by a blue “X”), centre of the 1st BCG. Moreover, the 1st BCG is extremely irregular in morphology, containing several distinct filamentary tidal-tail like features, which is very atypical of relaxed elliptical cD galaxies found in the cores of cluster environments. These filamentary structures are blue in colour, and possibly represent star forming regions related to an ongoing merger of two gas-rich galaxies (Fig. 11 left panel). Alternatively, these complex features might represent signatures of a vigorous active galactic nucleus (AGN) feedback process at work. We note that these filamentary structures are quite similar to those found near galaxy NGC 1275 in the core of the Perseus cluster (Whitmore & Schweizer 1995), or in the central galaxy of the cluster RXC J1504-0248 (Soja et al. 2018), or near NGC 4696 in the core of the Centaurus cluster (Crawford et al. 2005). This indicates that the central galaxy in MACS0417 is still dynamically active and has not yet attained the relaxed state of a giant cD galaxy found at the cluster centers.

In addition to the complex and filamentary optical structures near the central galaxy mentioned above, we discovered three other interesting ring-shaped objects seen in the HST image of the cluster. These are highlighted by green 5 arcsec \times 5 arcsec ($\sim 5.5 \times 5.5$ kpc²) boxes in Fig. 10 panel C, and marked by numbers 1 to 3. Their zoomed-in images are shown in panels B, D and E for more clarity. Close inspection of these objects reveals that they are strong gravi-

tationally lensed images of a single background galaxy, probably a distant star forming galaxy.

This interpretation is confirmed by the evident opposite parity of images 1 and 2 (panels B and D) and the same parity of images 1 and 3 (panels B and E) seen in Fig. 10. This means that a critical curve in the lens plane separates images 1 and 2 and also images 2 and 3 (images 1 and 3 are clearly of same parity). We have not been able to locate any other possible members of this multiply-image system. In addition, we report two other strong lensing features: a giant arc at 24 arcsec north of the 1st BCG and a smaller arc at 44 arcsec south of the 1st BCG (white ellipses in Fig. 11, right panel). It is very likely that more strong lensing features remain to be found in this field. Together with redshift measurements, modeling of the strong lensing features can be used to constrain the inner mass distribution, which is beyond the scope of the present paper.

5 DISCUSSION

In spite of the relatively poor seeing and low exposure times of the Subaru images, we have successfully derived the mass distribution of the bimodal merging system MACS0417 through the weak gravitational lensing technique. The recovered mass map (Fig. 2 “D”) shows an elongated structure with the peak corresponding to the main cluster lying very close to the position of the first BCG. This feature is also suggested by the numerical density distribution of the red sequence galaxies (Fig. 2 “B” and “C”), which also indicates that the dominant matter content of the subcluster surrounds the position of the second BCG. Corroborating previous X-ray based estimates, we found a very massive system with a total mass of $M_{200} = 13.8^{+2.6}_{-2.8} \times 10^{14} M_{\odot}$. Regarding the individual structures, the main cluster mass is evaluated as $M_{200}^c = 11.5^{+3.0}_{-3.5} \times 10^{14} M_{\odot}$, whereas for the subcluster the value is $M_{200}^s = 1.96^{+1.60}_{-0.95} \times 10^{14} M_{\odot}$. This analysis allowed us to compute the uncertainties on the centre of the main cluster mass distribution, and to compare that quantity with both the ICM (traced by its X-ray emission) and the distribution of the constituent galaxies (with the first BCG as their centroid). The identification of a possible detachment among these quantities is the base for models which explore a possible self-interaction behaviour of the dark matter (e.g. Harvey et al. 2015). However, our results have shown that the position of the main cluster mass centre, the corresponding X-ray peak and the 1st BCG are all comparable within 99% c.l. (Fig. 2 “E”), meaning that this structure has retained its gas content after the pericentric passage of the subcluster.

As far as the subcluster is concerned, a related ICM clump is not detected, suggesting that it can be disrupted due to the interaction with the main cluster. Therefore, MACS0417 can be classified as single dissociative merging cluster (Dawson 2013), where only the most massive component has retained its gas content as seen, e.g., in A1758 (Monteiro-Oliveira et al. 2017a). Future combined strong plus weak lensing analysis will improve our understanding of the mass distribution in the inner part of MACS0417. Additionally, future radial velocity surveys of the cluster members will also enable us to fully address the current dynamical state of this merger and determine the position of

the merger axis in relation to the plane of the sky. In addition, the reconstructed dynamical state can be used as an input for tailor-made hydrodynamical simulations aiming to explain the observed features in this interesting target.

The X-ray surface brightness profiles and detected edges imply that the density discontinuities seen in the ICM/IGM are related to either shock fronts or cold fronts, depending on the direction of the temperature jump (e.g., Markevitch & Vikhlinin 2007). Now, it is believed that the radio halos result from the re-acceleration of mildly relativistic electrons during a merger event between galaxy clusters (e.g., Brunetti et al. 2001; Petrosian 2001). MACS0417 hosts a radio halo elongated in the southeast – northwest (hereafter SE–NW) direction (Dwarakanath et al. 2011; Parekh et al. 2017).

We searched for surface brightness edges near the location of the radio halo. A sharp surface brightness edge is clearly visible in Fig. 5, located 45 arcsec \sim (255 kpc) towards SE direction from the center of the cluster, where a compact radio core of an AGN is also visible, which is superposed on the above radio halo. This unresolved radio core is possibly associated with the brightest central knot (an active galaxy nucleus) of the 1st BCG visible on the HST image, measured at position RA $04^h 17^m 34.7^s$, Dec. $-11^{\circ} 54' 32.3''$. The compact X-ray core is also visible in *Chandra* X-ray image, measured at position RA $04^h 17^m 34.56^s$, Dec. $-11^{\circ} 54' 30.0''$. The SE edge is best fitted by a broken power-law model with a density compression factor $C = 2.21 \pm 0.12$, and there is a temperature jump evidence that it is associated with a cold front. MACS0417 is a compact cool core merging cluster. Therefore, the cold front is most likely a sloshing driven cold front, similar to that of Abell 2142 (Rossetti et al. 2013) and A2052 (Machado & Lima Neto 2015). From Fig. 5, we can see that excess X-ray emission toward the SE direction is formed by the ICM of the core sloshing around the centre of MACS0417. We expect this excess emission region to be metal-rich and cooler than that of nearby regions from the centre of the cluster. Analyses of the temperature and metal abundance reveal that the region corresponding to the excess X-ray emission, associated to the SE cold front presented in §. 4.1.4, indeed has a lower temperature and higher metal abundance, $Z = 0.54 \pm 0.14 Z_{\odot}$, than other regions located at same distance from the centre, $Z = 0.29 \pm 0.12 Z_{\odot}$.

Parekh et al. (2017) found that the spectral index⁵ of the diffuse radio emission between 610 and 1575 MHz is $\alpha \sim -1.72$, and classified this source as an ultra-steep spectrum giant (~ 1.1 Mpc) radio halo. However, considering the central temperature, entropy and cooling time (Cavagnolo et al. 2009; Giacintucci et al. 2017), we have classified this source as a cool-core giant radio-halo-host cluster similar to CL1821+643 (Bonafede et al. 2014), A2390 and A2261 (Sommer et al. 2017). This makes MACS0417 one of the exceptionally rare cool core clusters hosting an ultra steep spectrum radio halo. Past studies have shown that giant radio halos are usually found in massive mergers and not in cool core clusters. On the other hand, a different class of radio sources, namely ‘radio mini haloes’

⁵ The radio flux density, S , is proportional to ν^{α} , where ν is the frequency of the observation and α is the spectral index.

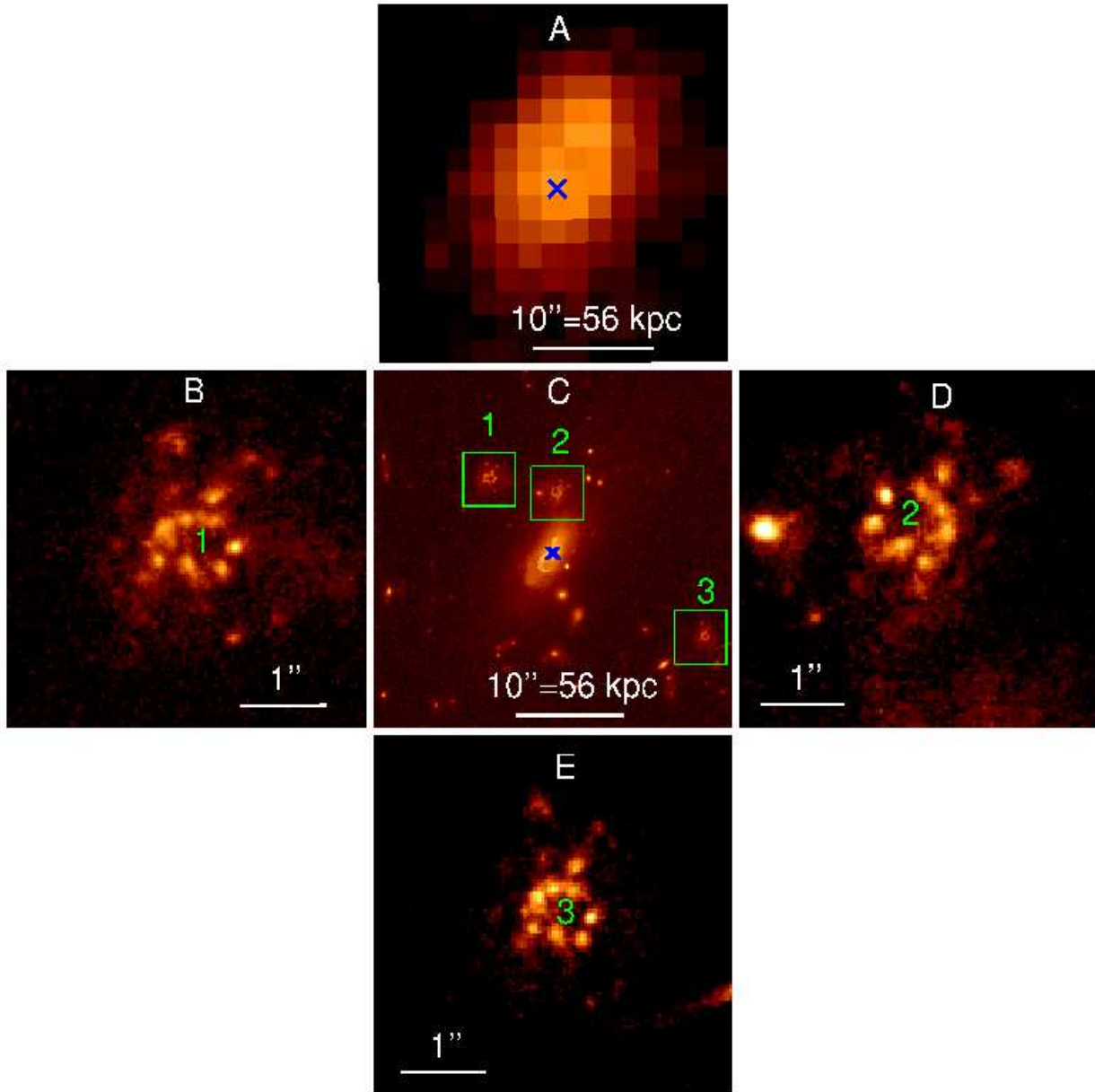


Figure 10. *A:* The *Chandra* 0.5–3.0 keV, exposure corrected, background subtracted *Chandra* X-ray image. The X-ray peak position is highlighted by a blue cross. *C:* HST high resolution (0.05 arcsec/pix) (F606W) V band filter optical image of the central (1st) BCG of MACS0417. The bright X-ray peak position is shown by blue cross. Peculiar circular type sources are highlighted by numbers 1 to 3 and their zoomed images are shown in panel B, D and E, respectively. The FOV of panel A and C is approximately 0.5 arcmin \times 0.5 arcmin² ($\sim 170 \times 170$ kpc²), while panel B, D and E have angular sizes 5 arcsec \times 5 arcsec ($\sim 5.5 \times 5.5$ kpc²).

are common in cool core clusters (Giacintucci et al. 2017). This brings up the possibility that the radio emission in MACS0417 could be generated by the same physical mechanism responsible for ‘radio mini haloes’, but on a much larger physical scale of 1.1 Mpc.

A spatial correlation has been observed between cold fronts and radio minihalos detected in a few galaxy clusters (Mazzotta & Giacintucci 2008), suggesting a connection between the sloshing motion of the gas and the origin of this kind of radio sources ZuHone et al. (2013). With the use of high-resolution MHD simulations, it has been shown that

gas sloshing can cause turbulent re-acceleration of relativistic electron seeds (e.g., from past AGN activity) and can produce diffuse steep-spectrum radio emission within the region of the sloshing cold front. The SE cold front and the radio halo in MACS0417 next to the sloshing cold front, extending towards the NE direction behind it, is quite consistent with this established scenario.

Another possibility is that the MACS0417 system could be an intermediate class, where a radio minihalo has been switched off because of the turbulent motions generated during the merger event, and the relativistic elec-

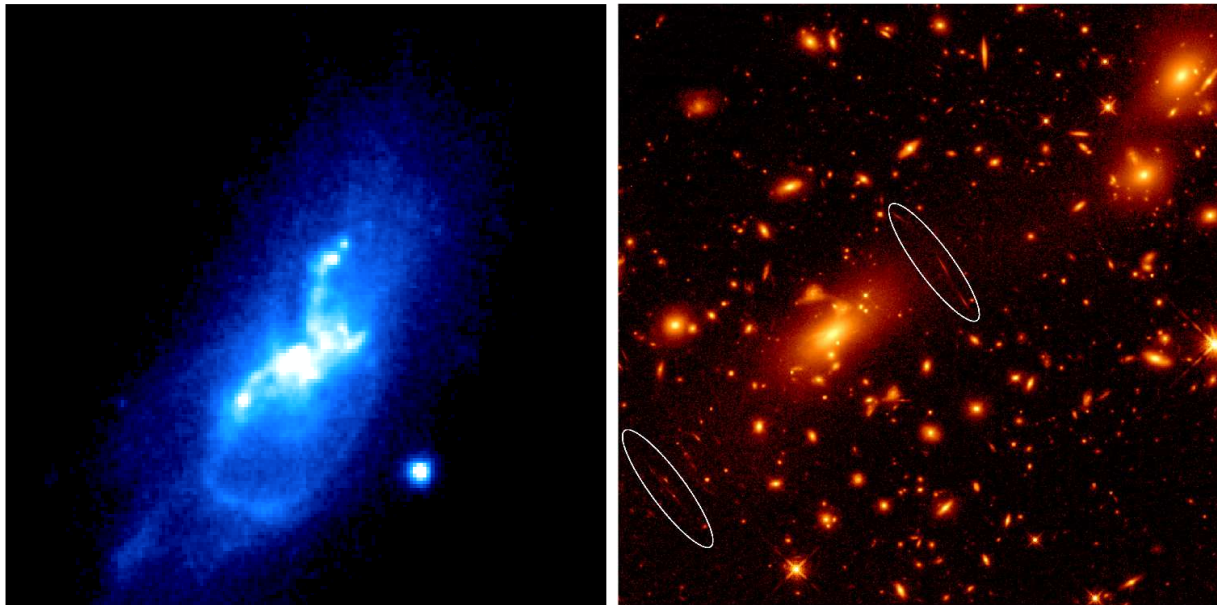


Figure 11. *left panel:* HST 10 arcsec \times 10 arcsec high-resolution UVIS V (F606W) band image. *Right panel:* A giant arc at ~ 24 arcsec and a smaller arc at ~ 44 arcsec are both evident in the HST 2.4 arcmin \times 2.4 arcmin IR H band (F160W) filter image and highlighted by white ellipses.

trons have been transported across larger distances than usual (Brunetti & Jones 2014). In this case, one should assume that the merger has dissipated enough energy to re-accelerate relativistic electron seeds (e.g., from past AGN activity), but not enough to disrupt the cool core.

6 CONCLUSION

We present observations of the merging cluster system MACS0417 using archival data obtained with *Chandra* (X-ray), Subaru, HST (optical), GMRT (low-frequency radio) and Bolocam (SZE 2.1 mm). From our analysis presented in this paper, we can draw the following conclusions.

(i) The weak lensing analysis of MACS0417, which is the first in the literature considering the system as the combination of a main cluster plus a subcluster, yields a mass ratio of $\sim 6:1$ of the two dark matter haloes. The individual masses are $M_{200}^c = 11.5^{+3.0}_{-3.5} \times 10^{14} M_{\odot}$ (main cluster) and $M_{200}^s = 1.96^{+1.60}_{-0.95} \times 10^{14} M_{\odot}$ (subcluster) leading to a total cluster mass of $M_{200} = 13.8^{+2.6}_{-2.8} \times 10^{14} M_{\odot}$.

(ii) MACS0417 is classified as a dissociative merger since the main cluster has retained its gaseous content as shown by the detected spatial coincidence (within 99% c.l.) of the distribution of the dark matter, ICM and member galaxy components. On the other hand, the subcluster seems to have had its gas content disrupted due to the merger.

(iii) The optical image of the first BCG shows interesting filamentary substructure, which is atypical of normal BCGs and may indicate an ongoing merger between the two galaxies.

(iv) We confirm a surface brightness edge to the east-south direction at a distance of 45 arcsec (~ 255 kpc) from

the centre of MACS0417, also reported by Botteon et al. (2018).

(v) The spectral analysis across the inner and outer regions of the edge has allowed us to confirm that this sharp emission edge is a cold front. The overall structure, surface brightness profile, temperature and metal abundance values point towards the presence of a sloshing induced cold front in this system.

(vi) We detect three components of a possible multiply-imaged strongly lensed background star forming galaxy, plus two previously unreported arcs which are all indications of strong lensing in this system. Strong lensing analysis of MACS0417 will lead to a clearer understanding of this cluster.

(vii) We find that the peak of the Sunyaev-Zel'dovich decrement of MACS0417 is displaced from its X-ray peak, which we interpret to be a consequence of the merger dynamics in the system.

ACKNOWLEDGMENTS

MBP gratefully acknowledges the support from following funding schemes: Department of Science and Technology (DST), New Delhi under the SERB Young Scientist Scheme (SERB/YSS/2015/000534), Department of Science and Technology (DST), New Delhi, and the INSPIRE faculty Scheme (DST/INSPIRE/04/2015/000108). MBP also wishes to acknowledge with thanks the support received from IUCAA, Pune, India in the form of their visiting Associate programme. RMO thanks very much the faculty members and staff of the Astronomy Department/Institut of Physics of the Federal University of Rio Grande do Sul for their lovely hospitality and the provided support which made

possible the continuity of this research. RMO also thanks Prof. Eduardo S. Cypriano (IAG/USP) for share his computational resources and Prof. Cláudia Lúcia M. Oliveira (IAG/USP) for the administrative support. ML acknowledges CNRS for its support. ML acknowledges CNRS and CNES for support. This research has made use of the data from *Chandra* Archive. Part of the reported results are based on observations made with the NASA/ESA Hubble Space Telescope, obtained from the Data Archive at the Space Telescope Science Institute, which is operated by the Association of Universities for Research in Astronomy, Inc., under NASA contract NAS 5-26555. This research has made use of software provided by the Chandra X-ray Centre (CXC) in the application packages CIAO, ChIPS, and Sherpa. This work is based on observations taken by the RELICS Treasury Program (GO 14096) with the NASA/ESA HST, which is operated by the Association of Universities for Research in Astronomy, Inc., under NASA contract NAS5-26555. This research has made use of NASA's Astrophysics Data System, and of the NASA/IPAC Extragalactic Database (NED) which is operated by the Jet Propulsion Laboratory, California Institute of Technology, under contract with the National Aeronautics and Space Administration. Facilities: Chandra (ACIS), HST (ACS). This work also is based on data collected at Subaru Telescope, which is operated by the National Astronomical Observatory of Japan.

REFERENCES

- Applegate D. E., et al., 2014, *MNRAS*, **439**, 48
- Bagchi J., Enßlin T. A., Miniati F., Stalin C. S., Singh M., Raychaudhury S., Humeshkar N. B., 2002, *New A*, **7**, 249
- Bagchi J., et al., 2011, *ApJ*, **736**, L8
- Bertin E., Arnouts S., 1996, *A&AS*, **117**, 393
- Bonafede A., et al., 2014, *MNRAS*, **444**, L44
- Botteon A., Gastaldello F., Brunetti G., 2018, *MNRAS*, **476**, 5591
- Bridle S. L., Hobson M. P., Lasenby A. N., Saunders R., 1998, *MNRAS*, **299**, 895
- Brunetti G., Jones T. W., 2014, *International Journal of Modern Physics D*, **23**, 1430007
- Brunetti G., Setti G., Feretti L., Giovannini G., 2001, *MNRAS*, **320**, 365
- Caccianiga A., Maccacaro T., Wolter A., Della Ceca R., Gioia I. M., 2000, *A&AS*, **144**, 247
- Cavagnolo K. W., Donahue M., Voit G. M., Sun M., 2009, *ApJS*, **182**, 12
- Clowe D., Gonzalez A., Markevitch M., 2004, *ApJ*, **604**, 596
- Coe D. A., RELICS Team 2017, in American Astronomical Society Meeting Abstracts. p. 205.05
- Crawford C. S., Hatch N. A., Fabian A. C., Sanders J. S., 2005, *MNRAS*, **363**, 216
- Dawson W. A., 2013, *ApJ*, **772**, 131
- Dickey J. M., Lockman F. J., 1990, *ARA&A*, **28**, 215
- Duffy A. R., Schaye J., Kay S. T., Dalla Vecchia C., 2008, *MNRAS*, **390**, L64
- Dwarakanath K. S., Malu S., Kale R., 2011, *Journal of Astrophysics and Astronomy*, **32**, 529
- Eckert D., Molendi S., Paltani S., 2011, *A&A*, **526**, A79
- Eckert D., et al., 2015, *Nature*, **528**, 105
- Feretti L., Giovannini G., Govoni F., Murgia M., 2012, *A&A Rev.*, **20**, 54
- Giacintucci S., Markevitch M., Cassano R., Venturi T., Clarke T. E., Brunetti G., 2017, *ApJ*, **841**, 71
- Harvey D., Massey R., Kitching T., Taylor A., Tittley E., 2015, *Science*, **347**, 1462
- Kale R., Dwarakanath K. S., 2012, *ApJ*, **744**, 46
- Kneib J.-P., Natarajan P., 2011, *A&A Rev.*, **19**, 47
- Machado R. E. G., Lima Neto G. B., 2015, *MNRAS*, **447**, 2915
- Mann A. W., Ebeling H., 2012, *MNRAS*, **420**, 2120
- Markevitch M., Vikhlinin A., 2007, *Phys. Rep.*, **443**, 1
- Markevitch M., Gonzalez A. H., Clowe D., Vikhlinin A., Forman W., Jones C., Murray S., Tucker W., 2004, *ApJ*, **606**, 819
- Marshall P. J., Hobson M. P., Gull S. F., Bridle S. L., 2002, *MNRAS*, **335**, 1037
- Martel H., Robichaud F., Barai P., 2014, *ApJ*, **786**, 79
- Martin A. D., Quinn K. M., Park J. H., 2011, *Journal of Statistical Software*, **42**, 22
- Mazzotta P., Giacintucci S., 2008, *ApJ*, **675**, L9
- Medezinski E., Broadhurst T., Umetsu K., Oguri M., Rephaeli Y., Benítez N., 2010, *MNRAS*, **405**, 257
- Mellier Y., 1999, *ARA&A*, **37**, 127
- Million E. T., Allen S. W., Werner N., Taylor G. B., 2010, *MNRAS*, **405**, 1624
- Monteiro-Oliveira R., Cypriano E. S., Machado R. E. G., Lima Neto G. B., Ribeiro A. L. B., Sodr e L., Dupke R., 2017a, *MNRAS*, **466**, 2614
- Monteiro-Oliveira R., Lima Neto G. B., Cypriano E. S., Machado R. E. G., Capelato H. V., Lagan a T. F., Durret F., Bagchi J., 2017b, *MNRAS*, **468**, 4566
- Nagai D., 2006, *ApJ*, **650**, 538
- Navarro J. F., Frenk C. S., White S. D. M., 1996, *ApJ*, **462**, 563
- Navarro J. F., Frenk C. S., White S. D. M., 1997, *ApJ*, **490**, 493
- Nulsen P. E. J., 1982, *MNRAS*, **198**, 1007
- Nychka D., Furrer R., Sain S., 2014, *Fields: Tools for spatial data*. <http://CRAN.R-project.org/package=fields>
- Oke J. B., 1974, *ApJS*, **27**, 21
- Ouchi M., et al., 2004, *ApJ*, **611**, 660
- Pandge M. B., et al., 2017, *MNRAS*, **472**, 2042
- Parekh V., Dwarakanath K. S., Kale R., Intema H., 2017, *MNRAS*, **464**, 2752
- Petrosian V., 2001, *ApJ*, **557**, 560
- Piffaretti R., Arnaud M., Pratt G. W., Pointecouteau E., Melin J.-B., 2011, *A&A*, **534**, A109
- Rossetti M., Eckert D., De Grandi S., Gastaldello F., Ghizzardi S., Roediger E., Molendi S., 2013, *A&A*, **556**, A44
- Sayers J., et al., 2013, *ApJ*, **768**, 177
- Schneider P., 2005, *ArXiv Astrophysics e-prints*,
- Scoville N., 2007, in Baker A. J., Glenn J., Harris A. I., Mangum J. G., Yun M. S., eds, *Astronomical Society of the Pacific Conference Series Vol. 375, From Z-Machines to ALMA: (Sub)Millimeter Spectroscopy of Galaxies*. p. 166
- Seitz S., Schneider P., Bartelmann M., 1998, *A&A*, **337**, 325
- Soja A. C., Sodr e L., Monteiro-Oliveira R., Cypriano E. S., Lima Neto G. B., 2018, *MNRAS*, **477**, 3279
- Sommer M. W., Basu K., Intema H., Pacaud F., Bonafede A., Babul A., Bertoldi F., 2017, *MNRAS*, **466**, 996
- Whitmore B. C., Schweizer F., 1995, *AJ*, **109**, 960
- Wright C. O., Brainerd T. G., 2000, *ApJ*, **534**, 34
- Yagi M., Kashikawa N., Sekiguchi M., Doi M., Yasuda N., Shimasaku K., Okamura S., 2002, *AJ*, **123**, 66
- Zacharias N., Monet D. G., Levine S. E., Urban S. E., Gaume R., Wycoff G. L., 2004, in *American Astronomical Society Meeting Abstracts*. p. 1418
- ZuHone J. A., Markevitch M., Brunetti G., Giacintucci S., 2013, *ApJ*, **762**, 78
- van Weeren R. J., et al., 2016, *ApJ*, **818**, 204
- von der Linden A., et al., 2014, *MNRAS*, **439**, 2